

Wurtzite Quantum Wires with Strong Spatial Confinement: Polarization Anisotropies in Single-Wire Spectroscopy

Viola Zeller¹, Nadine Mundigl,¹ Paulo E. Faria Junior¹, Jaroslav Fabian², Christian Schüller,¹ and Dominique Bougeard^{1,*}

¹*Institut für Experimentelle und Angewandte Physik, Universität Regensburg, Regensburg D-93040, Germany*

²*Institut für Theoretische Physik, Universität Regensburg, Regensburg D-93040, Germany*

(Received 9 May 2022; revised 29 July 2022; accepted 15 September 2022; published 4 November 2022)

We report GaAs/(Al, Ga)As nanowires in the one-dimensional (1D) quantum limit. The ultrathin wurtzite GaAs cores between 20 and 40 nm induce large confinement energies of several tens of millielectronvolts, allowing us to experimentally resolve up to four well-separated subband excitations in microphotoluminescence spectroscopy. Our detailed experimental and theoretical polarization-resolved study reveals a strong diameter-dependent anisotropy of these transitions: We demonstrate that the polarization of the detected photoluminescence is governed, on the one hand, by the symmetry of the wurtzite 1D quantum wire subbands but also, on the other, by the dielectric mismatch of the wires with the surrounding material. The latter effect leads to a strong attenuation of perpendicularly polarized light in thin-dielectric wires, making the thickness of the (Al, Ga)As shell an important factor in the observed polarization behavior. Including the dielectric mismatch to our $\mathbf{k} \cdot \mathbf{p}$ -based simulated polarization-resolved spectra of purely wurtzite GaAs quantum wires, we find excellent agreement between experiment and theory. These findings reveal insights relevant to spectroscopic studies of the 1D quantum regime and the design of photonic quantum wire applications such as lasers and hopefully open up paths for selective subband excitations.

DOI: 10.1103/PhysRevApplied.18.054014

I. INTRODUCTION

One-dimensional (1D) quantum wires stand out amongst spatially quantum confined solid-state structures because of their unique quantized properties, such as fully ballistic transport [1], efficient light-matter interaction with particular relevance for the realization of lasers [2,3], strong manifestations of correlation [4] or quasiparticle states [5], and dispersion effects [6] in spin-orbit coupled systems. At the same time, the experimental exploration of this rich physics is challenged by the availability of suitable solid-state structures. One challenge is the realization of wires with confinement energies large enough to operate experiments in the 1D quantum limit; in particular, for optical spectroscopy. In this regard, catalytically self-assembled ultrathin GaAs nanowires [7–10] with very pure crystal phases [11] have recently yielded interesting experimental perspectives. In this paper, we report 1D semiconductor quantum wires revealing up to four well-separated subband transitions in single-wire photoluminescence (PL) with confinement energies of several tens of millielectronvolts. Our core/shell nanowires feature ultrathin GaAs cores below 40 nm and an (Al, Ga)As shell for which we vary the

thickness. The experimental polarization-resolved spectra and observed confinement energies match very well with our $\mathbf{k} \cdot \mathbf{p}$ simulations for purely wurtzite nanowires, including band mixing in the valence bands. Our experimental and theoretical study also clearly demonstrates the importance of the (Al, Ga)As shell thickness in single-wire polarization-resolved studies: the *intrinsic* electronic polarization selection rules are overlain by *extrinsic* classical polarization anisotropies, resulting from the dielectric mismatch between the GaAs/(Al, Ga)As nanowire and its environment. We find that (Al, Ga)As shell thicknesses of several hundred nanometers are required to experimentally observe the pure wurtzite electronic 1D quantum wire polarization behavior for several quantum confined subbands.

II. EXPERIMENTAL AND THEORETICAL DETAILS

The investigated core/shell wurtzite GaAs quantum wires are grown by solid-source molecular-beam epitaxy (MBE) on semi-insulating GaAs(111)B substrates via Au-catalyzed vapor-liquid-solid growth. Prior to growth, the substrates are covered with a very thin Au layer of nominally 0.05 Å, which forms Au-Ga droplets of

*dominique.bougeard@ur.de

approximately 30-nm diameter. The nanowire growth procedure is separated into two steps. In the first step, we synthesize the ultrathin GaAs cores at a substrate temperature of 540 °C for 95 min, a Ga rate of 0.7 Å/s, and an As₄-to-Ga ratio of 2. This step yields vertically grown wires with high wurtzite crystal-phase purity [7,11,12], a uniform length of 2 μm on average, and an average diameter of 30 nm (± 10 nm), thin enough to observe 1D spatial quantum confinement effects [7]. In the second step, the growth temperature is lowered to 460 °C, while the As₄-to-Ga ratio is increased to approximately 4, enabling a lateral overgrowth of the ultrathin GaAs core with an Al_{0.38}Ga_{0.62}As shell. In this way, we fabricate several wafers with different (Al, Ga)As shell thicknesses. Figure 1 shows scanning electron micrographs (SEM) of as-grown nanowires without a shell [Fig. 1(a)] and with various shell thicknesses corresponding to a lateral overgrowth time of 13 min [Fig. 1(b)], 32 min [Fig. 1(c)], and 63 min [Fig. 1(d)]. All nanowire shells are finally capped with nominally 5 nm GaAs to prevent the oxidation of the (Al, Ga)As. We produce nanowires with total core/shell diameters ranging from 50 nm to 230 nm as determined by SEM, which we refer to as the *dielectric* diameter in the following, as the GaAs core and the Al_{0.38}Ga_{0.62}As

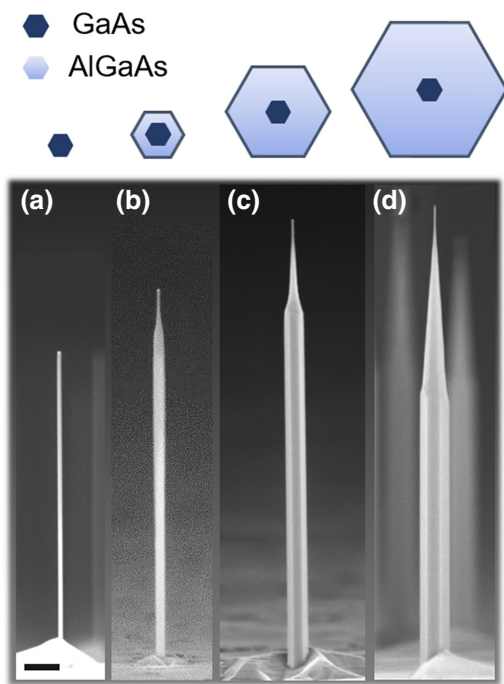


FIG. 1. Representative scanning electron micrographs of quantum wires from four different growth runs. Pure GaAs core (a) without a (Al, Ga)As shell and (b)–(d) with different (Al, Ga)As shell thicknesses. The total diameter of the wires amounts to (a) 30 nm, (b) 70 nm, (c) 160 nm, and (d) 220 nm, with lengths ranging from (a) 2 μm to (d) 3 μm. The scale bar is 250 nm.

shell have similar dielectric constants. The larger band gap of the Al_{0.38}Ga_{0.62}As shell confines all photocarriers to the GaAs core and suppresses nonradiative recombination caused by surface states, which is why we obtain a sufficient radiative efficiency in the photoluminescence (PL) even for the thinnest wires.

For PL experiments, the nanowires are randomly dispersed onto 300-nm thermal SiO₂ formed on *p*-doped silicon chips by carefully brushing the growth substrate over the chip surface. In our confocal microphotoluminescence (micrometer-PL) setup, the samples are excited by a pulsed semiconductor diode laser in a He-flow cryostat at 4.2 K. We use two different PicoQuant lasers with peak energies of 1.8 eV (690 nm) or 3.1 eV (405 nm), an approximately 50-ps pulse duration, and a variable repetition frequency. The laser beam is focused onto the sample through a 100× microscope objective with a numerical aperture of NA = 0.8, resulting in a spot diameter of approximately 1 μm, hence allowing us to address single nanowires lying on SiO₂. The PL signal is collected through the same objective and focused onto the entrance slit of a 75-cm spectrometer, dispersed by a 150-mm⁻¹ grating and detected with a charge-coupled device (CCD) camera. The exciting laser light is cut off by a suitable long-pass filter.

The conduction- and valence-band states of the pure GaAs wurtzite nanowires are calculated via the $\mathbf{k} \cdot \mathbf{p}$ framework, within the formalism of the envelope-function approximation and the plane-wave expansion to treat the hexagonal quantum confinement. The valence-band $\mathbf{k} \cdot \mathbf{p}$ Hamiltonian incorporates band-mixing effects of heavy, light, and crystal-field split-off holes, which are crucial to properly model the intrinsic polarization anisotropies of optical spectra [13–16]. The conduction band is treated with a parabolic dispersion. Specific details of the $\mathbf{k} \cdot \mathbf{p}$ -based calculations can be found in Refs. [7,17,18]. We use the valence-band parameters and the electron effective masses given in Ref. [19] [from the *GW*–local-density approximation (LDA) data set, without including the spin-splitting terms in the valence band].

The optical signatures of the different subband excitations in the nanowires are investigated by calculating the absorption spectra[20,21]:

$$\alpha^a(\hbar\omega) = C_0 \sum_{c,v,k_z} |p_{cvk_z}^a|^2 F_{cvk_z} \delta(\hbar\omega_{cvk_z} - \hbar\omega), \quad (1)$$

in which the superscript *a* refers to the light polarization along the *x* (perpendicular) or *z* (parallel to the nanowire axis) direction, the index *c(v)* labels the conduction (valence) subbands, *k_z* is the wave vector along the nanowire axis, $p_{cvk_z}^a = \langle c, k_z | \vec{p} \cdot \hat{a} | v, k_z \rangle$ is the dipole matrix element for the polarization of the light \hat{a} that incorporates the valence-band mixing and anisotropic Kane parameters [16,22], $F_{cvk_z} = (f_{v,k_z} - f_{c,k_z})$, $f_{c(v),k_z}$ is

the Fermi-Dirac distribution for the electron occupancy in the conduction (valence) subbands, \hbar is Planck's constant, ω_{cvk_z} is the interband transition frequency, and δ is the Dirac delta function. The constant C_0 is $C_0 = 4\pi^2 e^2 / (c_l n_r \epsilon_0 m_0^2 \omega \Omega)$, in which e is the electron charge, c_l is the speed of light, n_r is the refractive index of the material, ϵ_0 is the vacuum permittivity, m_0 is the free-electron mass, and Ω is the nanowire volume. In our calculations, we assume undoped systems at nearly zero temperature, so that $(f_{v\vec{k}} - f_{c\vec{k}}) = 1$ [23]. To include broadening effects due to the finite lifetimes of the carriers [20,24], we replace the Dirac delta function by a Lorentzian function with a full width at half maximum of 5 meV.

III. RESULTS AND DISCUSSION

We investigate several tens of single quantum wires with different core and shell diameters. These wires are optically preselected to display a defect-free emission, which is correlated with a high crystal-phase purity [11,12,25]. A characteristic excitation power series of the PL emission of a single wire is shown in Fig. 2(a). While at low excitation power the emission (light brown curve) only displays the single narrow PL peak representative of the ground-state emission [labeled "1" in Fig. 2(a)], up to four peaks, labeled "1" to "4," arise in the spectrum as we gradually increase the excitation power. Note that emission peaks 1–4 do not significantly change their energetic position with an increasing excitation level.

In Fig. 2(b), we summarize the peak energies observed in 37 single wires for the up to four peaks that arise with an increasing excitation power. These wires span core diameters between approximately 20 and 40 nm. The figure

displays the peak energies of peaks 2–4 as a function of the energy of their corresponding ground-state emission peak 1. As a consequence of increasing spatial quantum confinement, the ground-state PL energy of peak 1 continuously increases from 1.515 eV to 1.548 eV for decreasing core diameters. Furthermore, for all wires, the peak energies for peaks 2–4 clearly increase steadily, along with the corresponding ground-state energy. All three peak energies 2–4 follow a roughly linear evolution as a function of the ground-state energy 1, indicated as a guide to the eye for each peak in Fig. 2(b). The slightly larger scattering of the peak energies of peaks 3 and 4 is a result of some of these peaks being broader than peaks 1 and 2, increasing the error in our peak-value determination. The observed relationship of peaks 2–4 to peak 1 suggests that, like peak 1, the emission energies of peaks 2–4 are governed by the same core-diameter dependence for all 37 studied quantum wires. At the same time, we observe that for a given core diameter, the energies for peaks 1–4 are independent of the shell thickness, i.e., of the dielectric diameter of the wire. We interpret these observations as a strong indication for peaks 2–4 to represent emission peaks from excited quantum wire subbands, successively filled with an increasing excitation power. The confinement energies of several tens of millielectronvolts are exceptionally large for 1D quantum wires and, hence, particularly relevant for experimental studies of 1D phenomena. We emphasize that the 37 quantum wires shown in Fig. 2(b) feature different dielectric diameters. As a consequence, all the different shapes shown in Figs. 1(b)–1(d) are present in Fig. 2(b). Hence, while each wire in principle geometrically represents a cavity, we exclude peaks 1–4 to represent Fabry-Pérot resonances: we would be

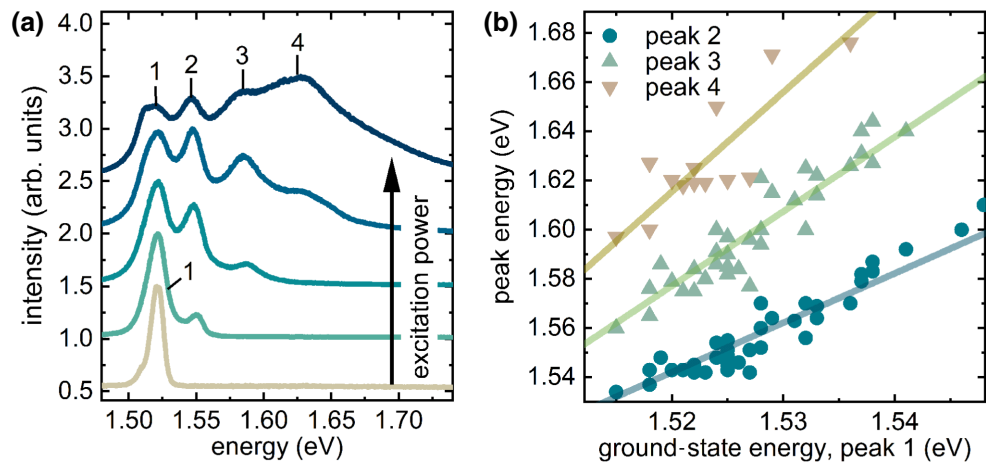


FIG. 2. The observation of subband transitions in wurtzite quantum wires. (a) Spectra of a single quantum wire at increasing excitation intensities. With higher excitation, the subbands gradually fill up and appear as discernible peaks in the PL spectrum. The individual spectra are normalized to their maximum. (b) The subband energies of the investigated nanowires at high excitation power as a function of the ground-state emission energy (at low excitation power). The linear dependence between the energies is indicative of subband transitions. The lines are guides for the eye.

highly unlikely to observe the behavior documented in Fig. 2(b) for Fabry-Pérot resonances in 37 wires with different dielectric diameters, tip shapes, and wire lengths.

The ability to resolve the emission of excited quantum wire subbands opens up the possibility of experimentally uncovering the polarization behavior of quantum wires in a wurtzite crystal. In bulk wurtzite GaAs, the degeneracy between the heavy-hole (hh) and light-hole (lh) valence bands is lifted. As a result, the PL emission of bulk nanowires has been shown to be dominated by transitions from the hh band, inducing a preferred polarization perpendicular to the nanowire axis [11,25–29]. Adding spatial quantum confinement, we have recently discussed a realistic model of the energetic subband structure of GaAs wurtzite quantum wires in the context of intersubband transitions resolved by resonant inelastic light scattering [18].

Figure 3(a) sketches the electronic subband structure of a 1D quantum wire for the conduction (gray), dominantly hh (red), and dominantly lh (blue) bands. Note that dominantly hh transitions (red) only contribute to emission and absorption with perpendicular dipoles, while lh transitions (blue) contribute to both perpendicular and parallel polarization. Hence, the character of the electronic transitions involved can be expected to strongly affect the polarization behavior of the experimental emission and absorption spectra.

In Fig. 3(b), we show the realistic simulation of a polarization-resolved absorption spectrum for a GaAs quantum wire with 26-nm core diameter. The spectrum is structured by the Van Hove singularities of the joint density of states for a 1D quantum object weighted by

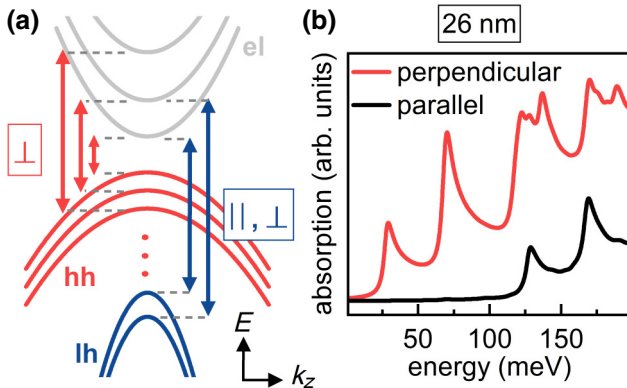


FIG. 3. The polarization selection rules in 1D-confined wurtzite GaAs. (a) A sketch of the subband dispersion resulting from size quantization. The electronic conduction band (gray) and the nondegenerate hh (red) and lh (blue) valence bands are split into subbands. The arrows indicate the allowed dipole transitions with their respective allowed directions of polarization. (b) Calculated polarization-resolved absorption spectra of a wurtzite GaAs nanowire with 26-nm core diameter, showing typical Van Hove singularities of a 1D quantum object.

the allowed optical transitions. These singularities are resonances of the transitions highlighted by the arrows in Fig. 3(a) and are offset with respect to the bulk wurtzite GaAs band gap, set here to $E_{\text{gap}} = 0$ meV. As can be seen in Fig. 3(b), our calculation for a wurtzite quantum wire with a 26-nm core diameter predicts the emission and absorption for energies up to 200 meV above the bulk wurtzite band gap to be dominated by perpendicular transition dipoles.

To test this prediction experimentally, we insert a rotatable linear polarizer in the detection path and analyze the polarization of the emitted light in the x and z directions. A schematic of the setup is shown in Fig. 4(a). We now discuss a series of quantum wires for which the energies of peaks 1–3 display excellent matches with the first Van Hove singularities in Fig. 3(b). From this excellent match between the simulation and the energy positions of the PL peaks, we conclude that all the wires discussed in the following have a core diameter of 26 nm.

In Fig. 4(b), we start with the polarization-resolved spectra (x and z directions) of a quantum wire that features a comparatively thin dielectric diameter of 45 nm, determined by SEM. In accordance with the predicted dominant hh character from our simulation, the polarization of the ground-state transition at 1.537 eV clearly shows a preferential direction perpendicular to the wire axis in the PL spectrum. Intriguingly, however, the dominant polarization of the emitted light changes from perpendicular to parallel at an energy of approximately 1.55 eV. The parallel polarized PL then clearly dominates the spectrum above

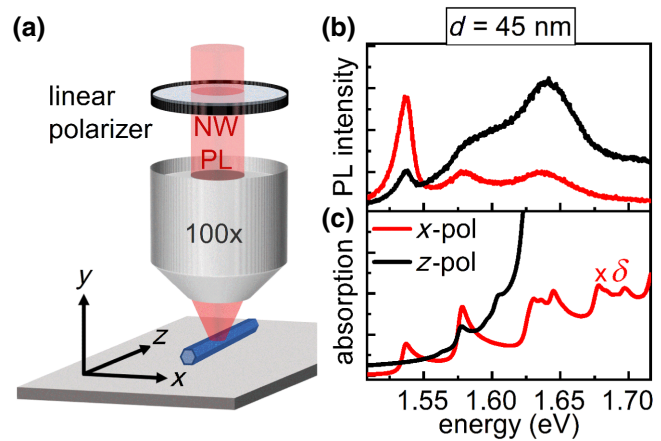


FIG. 4. The polarization-resolved analysis of thin quantum wires. (a) A simplified schematic of the measurement setup. (b) Experimental PL emission spectra analyzed perpendicular (x -pol., red) and parallel (z -pol., black) to the wire axis. (c) The calculated perpendicular- (red) and parallel- (black) polarized absorption spectra. The x -polarized spectrum (red) is multiplied by the attenuation constant $\delta = 0.016$ according to our simulations. The intensities in (b) and (c) are given in arbitrary units.

approximately 1.55 eV. Hence, at first sight, the polarization in the experiment is in discrepancy with our simulation in Fig. 3(b), which is solely based on interband transitions from the electronic 1D subband structure. Note, however, and as mentioned before, that the energetic positions of peaks 1–3 in Fig. 4(b) are in excellent agreement with Fig. 3(b).

This discrepancy in the polarization behavior between experiment and simulation motivates us to consider possible *extrinsic* impacts on the polarization behavior of the emission and absorption in nanowires and to explore whether they might add to or even outweigh the prediction of our *intrinsic* electronic simulation in certain energy regions of the spectrum. In this context, it has been discussed that the high aspect ratio, combined with the large refractive-index contrast between the wire and its environment (vacuum), causes a strong polarization anisotropy. This dielectric mismatch effect favors the absorption and emission of parallel polarized light. For instance, when a dielectric cylinder with the dielectric constant ϵ is placed into an external electric field E_0 , the component normal to the wire axis is essentially suppressed inside the wire [13,19,28,30,31]:

$$E_{\perp} = \frac{2\epsilon_0}{\epsilon + \epsilon_0} E_{0\perp}, \quad (2)$$

where ϵ_0 is the vacuum permittivity and E_{\perp} and $E_{0\perp}$ are the normal-electric-field components inside and outside the wire, respectively. At the same time, the field component parallel to the wire is not reduced: $E_{\parallel} = E_{0\parallel}$. Though Eq. (2) has been initially derived for static electric fields, it has been shown to also be valid for electromagnetic waves, as long as their wavelength can be considered to be much larger than the diameter of the wire, $\lambda \gg d$ [13,19,30,31]. Given that $E_{0\parallel} = E_{0\perp}$, the damping constant for the perpendicular field inside the wire amounts to

$$\delta = \frac{I_x}{I_z} = \frac{|E_{\perp}|^2}{|E_{\parallel}|^2} = \left| \frac{2\epsilon_0}{\epsilon + \epsilon_0} \right|^2. \quad (3)$$

Given that nanowires rarely fulfill the condition $\lambda \gg d$, we go beyond Eq. (3) by estimating the attenuation of the perpendicular electric field $\delta = I_x/I_y$ as a function of the nanowire diameter by finite-element-method- (FEM) based modeling (for a detailed description, see the Supplemental Material [32]). For the wire discussed in Fig. 4(b), we find that $\delta = 0.016$. Figure 4(c) then again displays our calculated absorption spectra discussed in Fig. 3(b) but, in addition, the x -polarized spectrum is now multiplied by $\delta = 0.016$, to take into account the dielectric mismatch effect for a wire with a diameter of 45 nm. We shift the absorption spectrum rigidly so that the first singularity coincides with the ground-state PL peak of Fig. 4(b). Clearly, the simulated absorption spectrum in Fig. 4(c)

predicts a preferred z polarization above 1.55 eV, while x polarization dominates below this energy. As a consequence, the simulation is now in excellent agreement with the characteristic features of the experimental emission spectra: not only do the energetic positions of the first four PL peaks match with the calculated electronic subband excitations but, also, the switching from a dominant x polarization to a dominant z polarization around 1.55 eV is correctly predicted. Clearly, the simulated absorption spectrum in Fig. 4(c) predicts a preferred z polarization above 1.55 eV due to hh-lh mixing [18], while x polarization dominates below this energy. Given that we excite with comparatively large power densities to pump up to four subband transitions, the experimental emission spectrum contains contributions from such mixed states. As a consequence, the simulation is now in excellent agreement with the characteristic features of the experimental emission spectra: not only do the energetic positions of the first four PL peaks match with the calculated electronic subband excitations but, also, the switching from a dominant x polarization to a dominant z polarization around 1.55 eV is correctly predicted. Note that we analyze several nanowires with dielectric diameters around 45 nm and observe this switching of the dominant polarization for all of them, even for core diameters smaller or larger than the discussed 26 nm. Hence, we interpret the strong attenuation of the perpendicular transitions in these wires as a consequence of strong dielectric mismatch.

Our model system of wurtzite GaAs quantum wires with variable shell thickness allows us to further specify the effect of the dielectric mismatch on the polarization behavior as a function of the dielectric diameter, as predicted by Ruda *et al.* [33]. In particular, the attenuation of the perpendicular-electric-field component should gradually be weakened when increasing the dielectric diameter. Thus, we now discuss the polarization-resolved spectra for a much thicker wire featuring a dielectric diameter of 220 nm. At the same time, compared to Fig. 4(b), we keep the GaAs quantum wire core diameter constant at 26 nm. From our FEM simulations, we calculate $\delta = 0.47$ for a dielectric diameter of 220 nm. In Fig. 5(a), we show the experimental polarization-resolved PL spectra and compare them to the corresponding calculated absorption spectra, plotted in Fig. 5(b). As in Fig. 4(c), the x -polarized simulated spectrum is multiplied by the attenuation factor, here $\delta = 0.47$. The three major PL peaks of the experiment agree very well with the first Van Hove singularities predicted for this 26-nm quantum wire core. At the same time, contrary to the thinner 45-nm dielectric diameter, this 220-nm dielectric diameter reveals a preferred polarization perpendicular to the wire axis over the entire experimentally covered energy range, consistent with the simulated absorption spectra.

Note that the experimental spectrum in Fig. 5(a) delivers a nonzero signal with parallel z polarization (black curve),

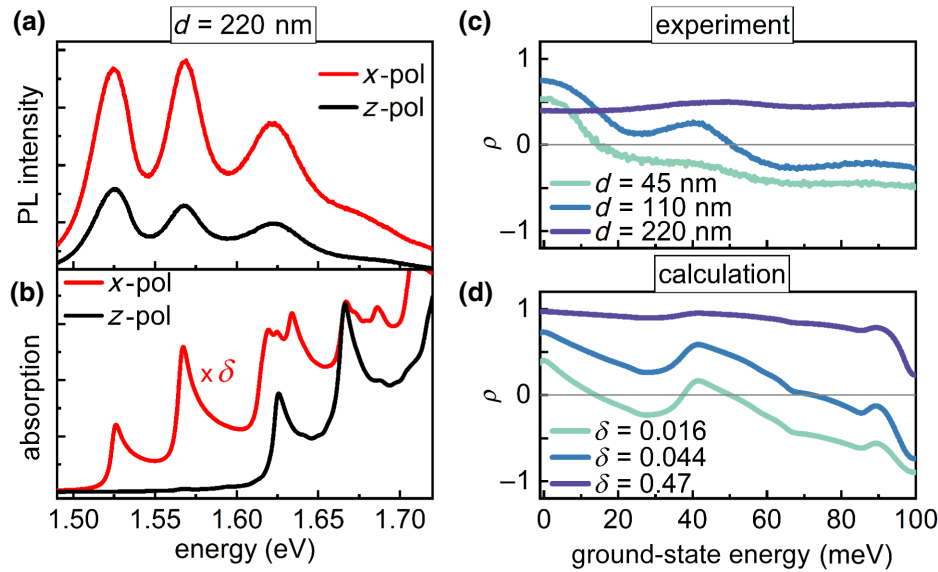


FIG. 5. (a) The polarization-resolved PL emission spectra of a quantum wire with a dielectric diameter of 220 nm and a core diameter of 26 nm. (b) The corresponding calculated absorption spectra of a 26-nm wire, where the x -polarized spectrum is multiplied by $\delta = 0.47$. The intensities in (a) and (b) are given in arbitrary units. (c) The energy-dependent ρ curves of three wires with a 26-nm core and different dielectric diameters of $d = 45$ nm, $d = 110$ nm, and $d = 220$ nm, respectively. (d) The energy-dependent ρ curves of the calculated absorption spectra with different δ values found from our FEM simulations for the corresponding diameters in (c).

including two peaks in the energy range of 1.50–1.60 eV, which are not predicted by the simulation in Fig. 5(b). As we discuss in more detail in the Supplemental Material [32], we see strong hints that the z -polarized signal in this comparatively thick wire actually does not result from z -polarized electronic transitions. Rather, it stems from y -polarized emission (which we do not directly access in our measurement geometry [Fig. 4(a)]), which propagates as a guided mode and is scattered isotropically at the end facets of the wire, producing a spurious z polarization. Given that the waveguiding of perpendicularly polarized light is more efficient for thicker dielectric wire diameters, we expect this scattering effect to be more pronounced in our wire with 220-nm diameter than in the 45-nm wire. Hence, the two peaks are clearly visible in the 220-nm wire in Fig. 5(a), while their occurrence is less obvious in the 45-nm wire in Fig. 4(b).

To demonstrate that the dominant modulation mechanism of the *intrinsic* polarization-resolved emission of our quantum wires is the dielectric diameter-dependent attenuation, we finally compare the 45 nm wire [Figs. 4(b) and 4(c)], the 220 nm wire [Figs. 5(a) and 5(b)], and a wire with an intermediate dielectric diameter thickness of 110 nm in Figs. 5(c) and 5(d) (constant core diameter, 26 nm). We plot the energy-dependent degree of linear polarization (ρ), defined as

$$\rho = \frac{(I_x - I_z)}{(I_x + I_z)}, \quad (4)$$

so that the pure x polarization of the light yields $\rho = +1$ and pure z polarization yields $\rho = -1$. Figure 5(c) shows the experimentally determined ρ for all three wires, as extracted from the polarization-resolved PL spectra. We compare these traces to the ρ extracted from our calculated absorption spectra shown in Fig. 5(d), for which the x polarization is modulated with the attenuation δ value corresponding to each dielectric diameter. In order to align the energy scale, the energy of the ground-state transition is set to zero for all curves.

For the comparatively thick-dielectric 220-nm wire ($\delta = 0.47$), which we analyze in Figs. 5(a) and 5(b), the preferred perpendicular polarization observed over the experimentally covered energy range translates into a ρ with a positive value and no significant variation as a function of energy, in both ρ curves in Figs. 5(c) and 5(d). The experimental and the simulated ρ only differ in their absolute values, the simulated one being close to 1 while the experimental one is smaller. We see here a quantitative manifestation of the scattering of y -polarized guided wire modes at the end facets of the comparatively thick wire (see the Supplemental Material [32]), which we discuss in the context of the corresponding spectra in Figs. 5(a) and 5(b). The ρ corresponding to the thinnest dielectric wire of 45 nm ($\delta = 0.016$), which we analyze in Figs. 4(b) and 4(c), nicely illustrates the previously discussed switching from a dominant x polarization (positive ρ) to a dominant z polarization (negative ρ) around 15 meV, as well as the presence of the first two subband transitions at 0 meV and 42 meV. Note also that the gradual

increase of the z -polarized emission from 0 to 100 meV, which is predicted in the model in Fig. 4(c) between 1.50 and 1.60 eV and which results from the increased contribution of hh-lh mixing [18], is clearly resolved in the experimental [Fig. 5(c)] and the simulated [Fig. 5(d)] ρ values. Hence, the ρ trace of the 45-nm wire points out the key consequence of the significant attenuation of the x -polarized emission due to the dielectric mismatch for sufficiently thin-dielectric wires: even small contributions from z -polarized transitions, which may seem negligible in the emission or absorption without an attenuation of the x polarization, will manifest in spectra of sufficiently thin wires. The control that we exert over the strength of the attenuation of the x -polarized contributions via the nanowire diameter is illustrated by the ρ of the intermediate 110-nm wire ($\delta = 0.044$): the sign change of the ρ occurs later in energy compared to the 45-nm wire. At the same time, the attenuation is still strong enough to clearly resolve the occurrence of the two first subband transitions and the increasing contribution of z -polarized transitions from 0 to 100 meV, with excellent consistency between the experimental [Fig. 5(c)] and simulated [Fig. 5(d)] ρ values. Note that the discrepancy of the absolute ρ values around 0 meV is much less pronounced for the 45-nm and the 110-nm wires than for the 220-nm wire. This observation supports our interpretation that the discrepancy for the 220-nm wire is due to significant scattering of perpendicular y -polarized guided wire modes, since waveguiding is not supported in the thinner wires. The excellent consistency between simulations and experiments highlights that the ρ spectra of the three nanowires are the result of a subtle superposition of the polarization behavior imposed by the electronic transitions and the attenuation of the perpendicular field components due to the diameter-dependent dielectric mismatch effect. Remarkably, the electromagnetic phenomenon of the dielectric mismatch effect and its attenuation of E_{\perp} allows to reveal even small contributions of the parallel-polarized transitions experimentally.

IV. CONCLUSIONS

In conclusion, our MBE-grown core/shell nanowires reproducibly provide ultrathin wurtzite GaAs cores. Such cores ease experiments in the 1D quantum limit [2–4,7,34], given their large confinement energies of several tens of millielectronvolts. We find excellent agreement between polarization-resolved photoluminescence spectra and $\mathbf{k} \cdot \mathbf{p}$ -based simulations for the excitation of up to four well-separated subband transitions. At the same time, while it does not modify the 1D quantum confinement of the GaAs core, we reveal a significant role of the thickness of the (Al, Ga)As shell in polarization-resolved spectroscopy of our quantum wires. The resulting polarization anisotropies will have to be integrated into spectroscopic studies and optically driven applications of such 1D wires.

Our experiments and simulations show that for shells below thicknesses around 200 nm, the dielectric mismatch effect will significantly overlie the intrinsic electronic 1D wurtzite selection rules. In practice, these thin-dielectric wires allow us to actively suppress perpendicularly polarized hh subband transitions and hence, at the same time, open up a path to the selective excitation of 1D lh excitons. Comparatively large shell thicknesses above 200 nm are required to observe the polarization behavior predicted by the electronic selection rules for up to four 1D subband excitations. Given the combination of large confinement energies provided by the ultrathin GaAs cores and the optical cavities, which can be designed via diameter control of the (Al, Ga)As shell, such thick-dielectric-diameter wires may be excellent candidates for the development of thresholdless quantum wire lasers. Our results provide insights into the design of such lasers; for example, in optimizing the overlap between the targeted electronic subband transition and the photonic cavity mode.

ACKNOWLEDGMENTS

We acknowledge the financial support of the Deutsche Forschungsgemeinschaft through Project ID 422 31469 5032-SFB1277 (Subprojects A01, B05, and B11).

- [1] B. J. van Wees, H. van Houten, C. W. J. Beenakker, J. G. Williamson, L. P. Kouwenhoven, D. van der Marel, and C. T. Foxon, Quantized Conductance of Point Contacts in a Two-Dimensional Electron Gas, *Phys. Rev. Lett.* **60**, 848 (1988).
- [2] E. Kapon, S. Simhony, R. Bhat, and D. M. Hwang, Single quantum wire semiconductor lasers, *Appl. Phys. Lett.* **55**, 2715 (1989).
- [3] M. Asada, Y. Miyamoto, and Y. Suematsu, Theoretical gain of quantum-well wire lasers, *Jpn. J. Appl. Phys.* **24**, L95 (1985).
- [4] V. V. Deshpande, M. Bockrath, L. I. Glazman, and A. Yacoby, Electron liquids and solids in one dimension, *Nature* **464**, 209 (2010).
- [5] J. D. Sau, S. Tewari, R. M. Lutchyn, T. D. Stanescu, and S. Das Sarma, Non-Abelian quantum order in spin-orbit-coupled semiconductors: Search for topological Majorana particles in solid-state systems, *Phys. Rev. B* **82**, 214509 (2010).
- [6] E. I. Rashba, Quantum nanostructures in strongly spin-orbit coupled two-dimensional systems, *Phys. Rev. B* **86**, 125319 (2012).
- [7] F. Dirnberger, M. Kammermeier, J. König, M. Forsch, P. E. Faria Junior, T. Campos, J. Fabian, J. Schliemann, C. Schüller, T. Korn, P. Wenk, and D. Bougeard, Ultralong spin lifetimes in one-dimensional semiconductor nanowires, *Appl. Phys. Lett.* **114**, 202101 (2019). [ArXiv:1809.08009](https://arxiv.org/abs/1809.08009)
- [8] N. Vainorius, S. Lehmann, A. Gustafsson, L. Samuelson, K. A. Dick, and M.-E. Pistol, Wurtzite GaAs quantum wires:

- One-dimensional subband formation, *Nano Lett.* **16**, 2774 (2016).
- [9] B. Loitsch, D. Rudolph, S. Morkötter, M. Döblinger, G. Grimaldi, L. Hanschke, S. Matich, E. Parzinger, U. Wurstabauer, G. Abstreiter, J. J. Finley, and G. Koblmüller, Tunable quantum confinement in ultrathin, optically active semiconductor nanowires via reverse-reaction growth, *Adv. Mater.* **27**, 2195 (2015).
- [10] P. Corfdir, H. Li, O. Marquardt, G. Gao, M. R. Molas, J. K. Zettler, D. van Treeck, T. Flissikowski, M. Potemski, C. Draxl, A. Trampert, S. Fernández-Garrido, H. T. Grahn, and O. Brandt, Crystal-phase quantum wires: One-dimensional heterostructures with atomically flat interfaces, *Nano Lett.* **18**, 247 (2018).
- [11] S. Furthmeier, F. Dirnberger, J. Hubmann, B. Bauer, T. Korn, C. Schüller, J. Zweck, E. Reiger, and D. Bougeard, Long exciton lifetimes in stacking-fault-free wurtzite GaAs nanowires, *Appl. Phys. Lett.* **105**, 222109 (2014).
- [12] F. Dirnberger, D. Abujetas, J. König, M. Forsch, T. Koller, I. Gronwald, C. Lange, R. Huber, C. Schüller, T. Korn, J. Sánchez-Gil, and D. Bougeard, Tuning spontaneous emission through waveguide cavity effects in semiconductor nanowires, *Nano Lett.* **19**, 7287 (2019).
- [13] J. Wang, M. S. Gudiksen, X. Duan, Y. Cui, and C. M. Lieber, Highly polarized photoluminescence and photodetection from single indium phosphide nanowires, *Science* **293**, 1455 (2001).
- [14] M. P. Persson and H. Q. Xu, Giant polarization anisotropy in optical transitions of free-standing InP nanowires, *Phys. Rev. B* **70**, 161310(R) (2004).
- [15] A. V. Maslov and C. Z. Ning, Radius-dependent polarization anisotropy in semiconductor nanowires, *Phys. Rev. B* **72**, 161310(R) (2005).
- [16] P. E. Faria Junior, T. Campos, and G. M. Sipahi, Interband polarized absorption in InP polytypic superlattices, *J. Appl. Phys.* **116**, 193501 (2014).
- [17] T. Campos, P. E. Faria Junior, M. Gmitra, G. M. Sipahi, and J. Fabian, Spin-orbit coupling effects in zinc-blende InSb and wurtzite InAs nanowires: Realistic calculations with multiband $\mathbf{k} \cdot \mathbf{p}$ method, *Phys. Rev. B* **97**, 245402 (2018).
- [18] S. Meier, P. E. Faria Junior, F. Haas, E.-S. Heller, F. Dirnberger, V. Zeller, T. Korn, J. Fabian, D. Bougeard, and C. Schüller, Intersubband excitations in ultrathin core-shell nanowires in the one-dimensional quantum limit probed by resonant inelastic light scattering, *Phys. Rev. B* **104**, 235307 (2021).
- [19] T. Cheiwchanwannajj and W. R. L. Lambrecht, Band structure parameters of wurtzite and zinc-blende GaAs under strain in the GW approximation, *Phys. Rev. B* **84**, 035203 (2011).
- [20] S. Chuang, *Physics of Optoelectronic Devices*, Wiley Series in Pure and Applied Optics (Wiley, New York, 1995).
- [21] M. Cardona and Y. Y. Peter, *Fundamentals of Semiconductors* Vol. 619 (Springer, Heidelberg, 2005).
- [22] P. E. Faria Junior, G. Xu, Y.-F. Chen, G. M. Sipahi, and I. Žutić, Wurtzite spin lasers, *Phys. Rev. B* **95**, 115301 (2017).
- [23] V. V. Ravi Kishore, B. Partoens, and F. M. Peeters, Electronic structure and optical absorption of GaAs/ $Al_xGa_{1-x}As$ and $Al_xGa_{1-x}As/GaAs$ core-shell nanowires, *Phys. Rev. B* **82**, 235425 (2010).
- [24] W. W. Chow and S. W. Koch, *Semiconductor-Laser Fundamentals: Physics of the Gain Materials* (Springer Science & Business Media, Heidelberg, 1999).
- [25] L. Ahtapodov, J. Todorovic, P. Olk, T. Mjåland, P. Slætnes, D. L. Dheeraj, A. T. Van Helvoort, B. O. Fimland, and H. Weman, A story told by a single nanowire: Optical properties of wurtzite GaAs, *Nano Lett.* **12**, 6090 (2012).
- [26] B. Ketterer, M. Heiss, E. Uccelli, J. Arbiol, and A. Fontcuberta i Morral, Untangling the electronic band structure of wurtzite GaAs nanowires by resonant Raman spectroscopy, *ACS Nano* **5**, 7585 (2011).
- [27] M. De Luca, A. Zilli, H. A. Fonseka, S. Mokkapati, A. Mirametro, H. H. Tan, L. M. Smith, C. Jagadish, M. Capizzi, and A. Polimeni, Polarized light absorption in wurtzite InP nanowire ensembles, *Nano Lett.* **15**, 998 (2015).
- [28] H.-Y. Chen, Y.-C. Yang, H.-W. Lin, S.-C. Chang, and S. Gwo, Polarized photoluminescence from single GaN nanorods: Effects of optical confinement, *Opt. Express* **16**, 13465 (2008).
- [29] T. Ba Hoang, A. F. Moses, L. Ahtapodov, H. Zhou, D. L. Dheeraj, A. T. J. van Helvoort, B.-O. Fimland, and H. Weman, Engineering parallel and perpendicular polarized photoluminescence from a single semiconductor nanowire by crystal phase control, *Nano Lett.* **10**, 2927 (2010).
- [30] L. Landau and E. Lifshitz, *Electrodynamics of Continuous Media*, 2nd ed., Course of Theoretical Physics, Vol. 8 (Pergamon, 1984).
- [31] H. E. Ruda and A. Shik, Polarization-sensitive optical phenomena in semiconducting and metallic nanowires, *Phys. Rev. B* **72**, 115308 (2005).
- [32] See the Supplemental Material at <http://link.aps.org/supplemental/10.1103/PhysRevApplied.18.054014> for the numerical FEM simulations and light scattering at nanowire end facets, including Refs. [35–39].
- [33] H. E. Ruda and A. Shik, Polarization-sensitive optical phenomena in thick semiconducting nanowires, *J. Appl. Phys.* **100**, 024314 (2006).
- [34] S. Furthmeier, F. Dirnberger, M. Gmitra, A. Bayer, M. Forsch, J. Hubmann, C. Schüller, E. Reiger, J. Fabian, T. Korn, and D. Bougeard, Enhanced spin-orbit coupling in core/shell nanowires, *Nat. Commun.* **7**, 12413 (2016).
- [35] I. H. Malitson, Interspecimen comparison of the refractive index of fused silica, *J. Opt. Soc. Am.* **55**, 1205 (1965).
- [36] C. Tan, Determination of refractive index of silica glass for infrared wavelengths by IR spectroscopy, *J. Non-Cryst. Solids* **223**, 158 (1998).
- [37] D. E. Aspnes, S. M. Kelso, R. A. Logan, and R. Bhat, Optical properties of $Al_xGa_{1-x}As$, *J. Appl. Phys.* **60**, 754 (1986).
- [38] J. Zheng, X. Yan, W. Wei, C. Wu, N. Sibirev, X. Zhang, and X. Ren, A low-threshold miniaturized plasmonic nanowire laser with high-reflectivity metal mirrors, *Nanomaterials* **10**, 1928 (2020).
- [39] D. Saxena, S. Mokkapati, P. Parkinson, N. Jiang, Q. Gao, H. H. Tan, and C. Jagadish, Optically pumped room-temperature GaAs nanowire lasers, *Nat. Photonics* **7**, 963 (2013).